Effects of Driving Conditions on Secondary Aerosol Formation from a GDI Vehicle Using an Oxidation Flow Reactor

Niina Kuittinen[1], Cavan McCaffery[2], Weihan Peng[2], Stephen Zimmerman[3], Patrick Roth[2], Pauli Simonen[1], Panu Karjalainen[1], Jorma Keskinen[1], David R. Cocker[2], Thomas D. Durbin[2], Topi Rönkkö[2], Roya Bahreini [*, 3], Georgios Karavalakis [*, 2]

[1]Aerosol Physics Laboratory, Physics Unit, Faculty of Engineering and Natural Sciences, Tampere University, Tampere, FI-33720, Finland

[2]University of California, Bourns College of Engineering, Center for Environmental Research and Technology (CE-CERT), 1084 Columbia Avenue, Riverside, CA 92507, USA

[3]University of California, Department of Environmental Sciences, 900 University Avenue, Riverside, CA 92521, USA

Abstract

A comprehensive study on the effects of photochemical aging on exhaust emissions from a vehicle equipped with a gasoline direct injection engine when operated over seven different driving cycles was assessed using an oxidation flow reactor. Both primary emissions and secondary aerosol production were measured over the Federal Test Procedure (FTP), LA92, New European Driving Cycle (NEDC), US06, and the Highway Fuel Economy Test (HWFET), as well as over two real-world cycles developed by the California Department of Transportation (Caltrans) mimicking typical highway driving conditions. We showed that the emissions of primary particles

* Corresponding Authors. Georgios Karavalakis, E-mail address: gkaraval@cert.ucr.edu

Roya Bahreini, E-mail address: bahreini@ucr.edu

were largely depended on cold-start conditions and acceleration events. Secondary organic aerosol (SOA) formation also exhibited strong dependence on the cold-start cycles and correlated well with SOA precursor emissions (i.e., non-methane hydrocarbons, NMHC) during both cold-start and hot-start cycles (correlation coefficients 0.95-0.99), with overall emissions of ~68-94 mg SOA per g NMHC. SOA formation significantly dropped during the hot-running phases of the cycles, with simultaneous increases in nitrate and ammonium formation as a result of the higher nitrogen oxide (NOx) and ammonia emissions. Our findings suggest that more SOA will be produced during congested, slow speed, and braking events in highways.

Keywords: Secondary aerosol; Gasoline direct injection; Oxidation flow reactor; Driving cycles; Primary emissions

1. Introduction

On-road gasoline vehicles are an important source of both gaseous and particulate emissions, including nitrogen oxides (NOx), volatile organic compounds (VOCs), black carbon, and particulate matter (PM). Tailpipe emissions of gasoline vehicles also include intermediate volatility organic compounds (IVOCs) and semivolatile organic compounds (SVOCs), including light molecular weight monoaromatic hydrocarbons, which are precursors for the production of secondary organic aerosol (SOA) through photooxidation reactions in the atmosphere (Kroll and Seinfeld, 2008; Robinson et al., 2007; Drozd et al., 2019). It has been demonstrated that SOA is the largest component of ambient organic aerosol (OA), followed by primary organic aerosol (POA) emitted as PM from anthropogenic and biogenic sources (Robinson et al., 2007; Jimenez et al., 2009). Previous studies suggest that gasoline vehicles dominate SOA formation in urban areas and significantly exceed the contribution of modern technology diesel vehicles (Gentner et al., 2017; Bahreini et al., 2012; Jathar et al., 2017; Platt et al., 2017).

Vehicle emissions are significantly influenced by driving conditions (Maricq et al., 2017; Herrington et al., 2012). This is especially true for vehicles equipped with gasoline direct injection (GDI) engines, where fuel is directly injected into the combustion chamber leading to fuel impingement and localized pool fires, causing diffusive combustion and soot generation (Duronio et al., 2020). These phenomena are more important during cold-start operation, which favors the formation of unburned hydrocarbons from the fuel and lubricating oil, as well as compounds that can act as SOA precursors upon atmospheric dilution and evaporation (Karjalainen et al., 2016). Recent studies have shown elevated tailpipe SVOC emissions from gasoline vehicles during cold-start operation compared to highway cruise conditions (Herrington et al., 2012; Miersch et al., 2019; Zimmerman et al., 2019).

Several studies have investigated the impact of gasoline vehicles on SOA formation using environmental smog chambers, either using transient driving cycles on a chassis dynamometer (Saliba et al., 2017; Vu et al., 2019; Zhao et al., 2017; Platt et al., 2013; Roth et al., 2020) or steady-state and idling driving conditions (Nordin et al., 2013; Liu et al., 2015; Kari et al., 2019; Zhang et al., 2020). The general consensus among these studies is that SOA mass exceeds POA mass (Vu et al., 2019; Nordin et al., 2013; Roth et al., 2020; Gordon et al., 2014). Vu et al. (2019) reported elevated levels of inorganic aerosol formation in the form of ammonium nitrate and several orders of magnitude higher SOA mass than primary PM after introducing the exhaust of four current GDI vehicles operated on the LA92 cycle into a chamber. Zhang and co-workers (2020) found that during idling conditions representing traffic congestion, higher concentrations of reactive aromatics and alkenes were present in the exhaust resulting in higher SOA formation potential compared to steady-state cruising conditions. Gordon et al. (2014) tested gasoline vehicles of a wide variety of model years and emission certification levels using a smog chamber and showed

greater SOA formation for the cold-start tests than the hot-start tests. They also showed lower SOA formation from newer vehicles compared to older technology vehicles. Other studies have shown that more volatile and semivolatile aromatic hydrocarbons present in gasoline are major emitted precursors for SOA formation from GDI vehicles (Roth et al., 2020; Nordin et al., 2013; Du et al., 2018; Peng et al., 2017).

An alternative methodology to batch chamber reactors for the characterization of SOA formation from combustion sources is the potential aerosol mass (PAM) oxidation flow-through reactor, which was developed to simulate concurrent SOA forming potential from highly transient conditions (Kang et al., 2007; Lambe et al., 2011). Oxidation flow reactors can be used in vehicle chassis dynamometer studies to capture the rapidly changing driving conditions during a driving cycle, as well as in field experiments (Cao et al., 2020; Tkacik et al., 2014). A recent investigation of a Euro 6 GDI vehicle using an oxidation flow reactor showed elevated levels of SOA mass during the cold-start New European Driving Cycle (NEDC) compared to the hot-start NEDC, especially during the first 200 seconds of the urban phase of the test cycle (Simonen et al., 2019). They also showed a comparable amount of ammonium nitrate formation to SOA formation, which is consistent with previous chamber studies of GDI vehicles. Other studies of GDI vehicles utilizing oxidation flow reactors have also shown a strong contribution of cold-start conditions on SOA formation (Karjalainen et al., 2016; Pieber et al., 2018; Simonen et al., 2017). Zhao et al. (2018) tested 16 gasoline vehicles, including GDI and port fuel injection (PFI) vehicles, over the cold-start LA92 cycle using a PAM reactor and found more SOA formation during cold-start operation because of the substantially higher gaseous organic emissions. They also showed similar SOA formation from GDI and PFI vehicles certified to the same emission standards.

In this study, the primary emissions and SOA formation potential from a current GDI vehicle were assessed, after introducing its dilute exhaust into an oxidation flow reactor and when operating on different driving cycles. A mixture of cold-start and hot-start certification driving cycles used in the United States (US) and Europe were employed, as well as real-world non-regulatory driving cycles that were developed to mimic driving conditions in California highways. This is one of the very few studies focusing on the effects of multiple driving conditions, including cold-start, hot-start, aggressive driving, and high-speed driving, on SOA formation from a GDI vehicle.

2. Experimental

2.1 Test vehicle and driving cycles

Testing was performed on a 2016 model year passenger car equipped with a 2.4-liter, 4-cylinder, wall-guided fuel injection system, a three-way catalyst (TWC), and operated with an overall stoichiometric air-fuel ratio. The engine had a rated horsepower of 185 hp at 6000 rpm, a torque of 178 ft-lbs. at 4000 rpm, and a compression ratio of 10:1. The vehicle was certified to meet the California LEVIII SULEV 30 emissions standard and had accumulated 31406 miles. Testing was performed with a typical California E10 fuel.

The vehicle was exercised in duplicate runs over several different driving cycles, including regulatory and non-regulatory driving schedules. Testing was conducted over the Federal Test Procedure (FTP), the New European Driving Cycle (NEDC), the LA92, the US06 Supplemental Federal Test Procedure, and the Highway Fuel Economy Test (HWFET) cycle. In addition, two driving schedules developed by the California Department of Transportation (Caltrans) to better represent typical driving patterns on California freeways were employed. The cycles (referred to as Caltrans 1 and Caltrans 2) were derived from field driving data representative of freeway,

arterial, collector road, and local driving, and traffic congestion levels typically found on Los Angeles freeways. More information about these test cycles are provided in the Supplementary Material (SM, Figure SM1).

2.2 Emissions testing

Gaseous and particulate emissions measurements were conducted in CE-CERT's Vehicle Emissions Research Laboratory (VERL), on a Burke E. Porter 48-inch single-roll electric dynamometer. A Pierburg Positive Displacement Pump-Constant Volume Sampling (PDP-CVS) system was used to obtain standard bag measurements for total hydrocarbons (THC), carbon monoxide (CO), nitrogen oxides (NOx), non-methane hydrocarbons (NMHC), and carbon dioxide (CO_2). All gaseous emissions were determined according to US EPA protocols for light-duty emission testing as given in the CFR, Title 40, Part 86. Tailpipe real-time soot or black carbon emissions were measured using an AVL Micro-Soot Sensor (MSS), which was further diluted by an additional dilutional tunnel. Particle size distributions were obtained using an Engine Exhaust Particle Sizer (EEPS) spectrometer in parallel with the MSS. The EEPS (TSI 3090, firmware version 8.0.0) was used to obtain real-time, second-by-second size distributions between 5.6 to 560 nm. Particles were sampled at a flow rate of 10 L/min, which is considered to be high enough to minimize diffusional losses. The dilution factor in CVS compared to the raw exhaust was a factor of 8.2-15.5.

2.3 Photooxidation Experiments

A novel oxidation flow reactor, the Tampere Secondary Aerosol Reactor (TSAR) was installed to the setup following an ejector diluter and was utilized to study secondary aerosol formation potential during transient driving conditions. TSAR is an OFR254-type oxidation flow reactor consisting of a residence time chamber, an oxidation reactor, an ozone generator, and an expansion

tube connecting the residence time chamber and oxidation reactor. Mass flow controllers were applied for flow control. TSAR has been designed to measure potential secondary aerosol formation from rapidly changing emission sources and it has nearly laminar flow conditions. In TSAR, the diluted exhaust is mixed with ozone, and the relative humidity (RH) of the sample is increased by mixing it with humidified air. The CVS and ejector diluter combined with dilution by ozone and humidified air flows resulted in total dilution of the sample by factors of 45-172 before entering the TSAR. The sample then passes through a residence time tube before entering an oxidation region where it is exposed to 254 nm UV radiation, which induces production of OH radicals through the photolysis of ozone in the presence of H_2O. The precursor gases present in the exhaust react with OH or O_3 to produce lower volatility molecules that then transfer to particle phase and produce secondary aerosol. The experimental setup with the TSAR is described in detail in SM and detailed information about the TSAR can be found elsewhere (Simonen et al., 2019; Simonen et al., 2017).

An average photooxidation timescale of 6.4 days was explored in this study (Table SM1, SM). The photooxidation time-scale falls within the timescales found to simulate peak SOA formation by Tkacik et al. (2014) of 2-3 days, Ortega et al. (2016) of 1-11 days, Saha et al. (2018) of 2-10 days, and Liu et al. (2019) of 1-3 days. Because the photooxidation timescale varied within a drive cycle (lowest during cold-starts, see SM) and because adjusting the conditions was not possible within a cycle, same conditions were applied for all cycles. The OH exposure and corresponding atmospheric age of the sample after oxidation was estimated by applying a chemical reaction model which considers OH suppression in the TSAR, similarly to Simonen et al. (2017).

The mini Aerodyne Aerosol Mass spectrometer (mAMS), equipped with a compact time-of-flight mass spectrometer mass resolution (i.e., $m/\Delta m$ with m being the nominal m/z and Δm the full

width at half-maximum) of ~1100 and mass accuracy better than 20 ppm), sampled downstream of the flow reactor to determine the non-refractory (NR) composition (OA, sulfate, nitrate, and ammonium) of the submicron aerosol particles (Jayne et al., 2000; Vu et al., 2016). Aerosol particles were sampled only in the mass spectrum mode, with a 7-8 s time resolution. Data from the mAMS were analyzed using Wavemetrics Igor Pro. (Squirrel ToF-AMS analysis toolkit v. 1.60 with PIKA module 1.20) following standard procedures outlined in previous studies (Bahreini et al., 2012b). Given the variable concentration of CO_2 in the vehicle exhaust, gas-phase background CO_2 was subtracted from the OA mass spectra using the measured gas-phase CO_2 concentrations from the CVS and the recommendation by Collier and Zhang (2013). Except for ammonium, high-resolution analysis of the mass spectra was used to generate the mass concentration of the other species. A composition-dependent collection efficiency factor was used to correct for particle bounce on the vaporizer (Middlebrook et al., 2012). Information about the methods used to determine the hydrocarbon-like organic aerosol (HOA) and the oxidation state of OA are shown in SM. In this study, SOA was determined as the difference between total measured organics and the estimated HOA by mAMS. It is worth noting that we cannot distinguish between SOA that is formed from oxidation of primary HOA versus those formed from gas to particle partitioning of low-volatility gaseous oxidation products.

The particulate mass of the aged aerosol, i.e., the aerosol sample treated with TSAR, was measured by electrical low-pressure impactor (ELPI+, Dekati Ltd.). The aerosol mass was calculated by integrating the size distribution over stages 3-7, corresponding to particle aerodynamic cut-off diameters between 30 to 604 nm. In the absence of full composition measurements of the primary aerosols, unit density of 1 g/cm^3 was used in the mass calculations, similar to the approach taken previously (Simonen et al., 2017; Simonen et al., 2019).

3. Results and Discussion

3.1 Particle size distributions

The average particle size distributions and real-time soot mass emissions for the test vehicle when operated on the NEDC, LA92, Caltrans 1, and Caltrans 2 cycles are presented in Figure 1. The particle size distribution data for the FTP is shown in Figure SM4 (SM). Particle size data for the US06 and HWFET cycles was not available, but their soot mass emissions are shown in Figure SM5 (SM). For the FTP, LA92, and NEDC cycles, the cold-start phase dominated the soot mass emissions and accumulation mode particle concentrations. During the first 50 s of these cycles, accumulation mode particle populations ranged between 40-200 nm in diameter, with geometric mean diameter (GMD) of the number size distribution varied between 20-110 nm. For the FTP and NEDC, particles gradually shifted to lower sizes (GMD of 30-60 nm) and concentrations after 100 s in the cycle. Overall, the cold-start cycles exhibited a decidedly bimodal particle size distribution across all phases. The accumulation mode dominated the particle size distribution, with lower concentrations of nucleation mode particle peaks centered about 20-30 nm in diameter. The elevated accumulation mode particle concentrations and soot mass emissions during the cold-start period can be attributed to the incomplete fuel vaporization when directly injected into the cold combustion chamber surfaces and the cold piston crown, which can lead to increased fuel impingement and localized pockets of liquid fuel (pool fires) (Duronio et al., 2020; Cheng et al., 2001; Yang et al., 2019). This fuel will burn in diffusion flames where soot formation initially takes place. Further, incomplete combustion byproducts, such as semi-volatile hydrocarbon fragments, will be less efficiently oxidized, due to the TWC being below its light-off temperature. Accumulation mode particles in GDI engines consist of carbonaceous chain agglomerates formed in local rich-fuel zones. Our results agree with previous studies with GDI vehicles that have shown

substantially higher accumulation mode particles and soot mass emissions during cold-start conditions (Yang et al., 2019; Chen et al., 2017).

It is evident that accumulation mode particle concentrations and soot mass emissions significantly decreased during the urban and hot-start phases of the FTP and LA92, but not during the entire duration of the UDC (urban driving cycle) segment of NEDC. For the UDC segment, accumulation mode particles were clearly found in relatively high concentrations during the acceleration hills of the UDC, with broader sizes ranging from 40-110 nm. Nucleation mode particles in modal sizes of 5-15 nm were also present throughout the duration of the UDC, owing their formation to the acceleration events, as transients disrupt the control of the global air-fuel ratios and exacerbate the heterogeneity of the cylinder charge. For the EUDC (extra-urban driving cycle) segment, both nucleation and accumulation mode particles were observed in lower concentrations than the UDC, with the major peaks appearing at the two main acceleration hills of the EUDC. Nucleation mode particles were likely derived mostly from semi-volatile hydrocarbon species via condensation, however, they can also have non-volatile fraction. Previous studies have indicated that GDI engines can emit small non-volatile particles that can act as condensation nuclei for semi-volatile exhaust compounds (Pirjola et al., 2015; Sgro et al., 2012). For the FTP and LA92 cycles, accumulation mode particle concentrations dropped for the urban and hot-start phases as a result of the engine warm-up, which led to steadily higher combustion temperatures and better fuel vaporization, avoiding pool fires responsible for soot formation. While accumulation mode particle populations were found in lower levels than those of the UDC, they spiked during the steeper acceleration periods of both the FTP and LA92 urban and hot-start phases. For the LA92, the GMD of the distribution remained between 50-120 nm until the hot-start phase during which GMD was generally at 40-50 nm. For the hot-start Caltrans cycles, particle concentrations across all size

ranges were lower than the cold-start cycles. For Caltrans 1 cycle, the nucleation mode dominated the particle size distribution profile, showing excessive populations of smaller nucleation mode particles in the 5-30 nm size range over the high-speed phase (GMD of around 20 nm) compared to the low speed phase (GMD decreased from 150 nm to 40 nm). Higher populations of accumulation mode particles were seen for Caltrans 2, with the nucleation mode particles being practically eliminated, except for some spikes during accelerations towards the end of the high-speed phase and GMD varied between 15-45 nm over the cycle. We theorize that the intense nucleation burst during high speed and load conditions was likely due to the higher exhaust gas temperature and the enhanced formation of sulfuric acid (Karjalainen 2014). Maricq et al. (2017) suggested that at high speed conditions of GDI vehicles, the time available for soot maturation is reduced, since the engine runs slightly rich to produce soot. These conditions could also promote the formation of small nanoparticles from semi-volatile hydrocarbons instead of their condensation onto soot particles (Maricq et al., 2017).

3.2 Aged aerosol

Figure 2 and Figure 3 show the real-time evolution of aged aerosol PM, OA, HOA, and sulfate, nitrate, and ammonium ions, as well as tailpipe NOx and NMHC emissions during operation over the LA92, NEDC, Caltrans 1, and Caltrans 2 cycles, respectively. Results for the FTP, HWFET, and US06 cycles are shown in Figures SM6-SM8, SM. For comparison purposes, primary PM corrected with time-delay of the signal in TSAR reactor are also presented. For both the LA92 and NEDC, aged PM were significantly higher than primary PM during the entire duration of the test cycle. The cold-start, and especially the first 150-200 seconds, showed a pronounced influence on the formation of aged PM, being more than 2 times higher in concentration than primary PM. The cold-start period also showed significantly higher concentrations of both primary and aged PM

when compared to the hot-running phases of both cycles, with aged PM formation being affected by vehicle acceleration events. Both hot-start Caltrans cycles followed the same patterns as the cold-start cycles and showed substantially higher aged PM concentrations than primary PM. The larger difference between primary and aged PM was likely due to the absence of a cold-start period for these cycles, which led to more complete combustion and lower formation of in-cylinder soot emissions, as seen in Figure 1. Overall, our results agree with previous studies on gasoline vehicles that have reported higher aged PM than primary PM emissions (Karjalainen et al., 2016; Vu et al., 2019; Simonen et al., 2019; Pieber et al., 2018; Zhao et al., 2018). For Caltrans 1, the low speed phase that represents congested highway driving resulted in elevated concentrations of aged PM compared to the relatively steady-state high-speed highway driving conditions. Similar findings with the TSAR have been previously reported, where lower concentrations of aged PM were found during long steady-state driving (Simonen et al., 2017). For the more aggressive Caltrans 2 cycle, overall aged PM was seen in higher concentrations than those of Caltrans 1, as a result of the heavier acceleration conditions of this cycle. The lower speed but more aggressive first phase of Caltrans 2 generated more aged PM than the higher speed but less aggressive phase 2. Phase 4 with the highest speed profile showed generally more aged PM than phase 3 that has slightly lower speed conditions.

Driving cycle showed a strong influence on the time-series of SOA formation. The largest contributor to SOA production was the first 200 seconds of the cold-start periods. During the cold-start period for both the LA92 and NEDC cycles, as well as for the FTP (Figure SM6, SM), SOA mass was considerably higher than during the hot-running phases, and correlated well (correlation coefficient of 0.99) with the tailpipe NMHC emissions (Figure SM9) despite the fact that not all species of the NMHCs are SOA precursors. Cold-start measurements indicate average formation

of 86 mg SOA/g NMHC while the overall weighted SOA formation in these cycles was lower at 68 mg SOA/g NMHC. Higher SOA formation from gasoline vehicles during cold-start operation has been reported in other studies using oxidation flow reactors (Karjalainen et al., 2016; Simonen et al., 2019; Pieber et al., 2018). The higher SOA formation during the cold-start period can be ascribed to the TWC being below its light-off temperature and therefore not efficient in oxidizing unburned fuel and lubricant oil hydrocarbon fragments and other VOCs, which are all known as SOA precursor emissions (Drozd et al., 2019). Similar observations were made by Saliba et al. (2017) when they found that cold-start THC emissions from SULEV vehicles equaled on average 101.5 miles of hot-stabilized driving. Typical gasoline fuels are dominated by single-ring aromatics in the range of C6-C12, with benzene, toluene, ethylbenzene, and xylenes being the predominant species, as well as straight-chain and branched alkanes (smaller than C8). Emissions of the small aromatic species can be attributed to unburned fuel or partially burned heavier aromatics, which are usually more difficult to evaporate than other hydrocarbon compounds (i.e., paraffins, olefins, etc.) during cold-start conditions in GDI combustion (Yang et al., 2019b). Detailed composition of the NMHC was not measured; however, consistent with previous studies, our results suggest a greater contribution of light aromatics in SOA formation during cold-start conditions that led to higher SOA formation per mass of NMHC (Roth et al., 2020; Nordin et al., 2013; Peng et al., 2017).

Although the maximum OA values changed during the cold-start period depending on the drive cycle, the oxidation characterization of OA remained similar. As seen in Figure SM10a, f_{44} (fraction of ions related to highly oxygenated organic species, CO_2^+) and f_{43} (fraction of ions predominantly related to mildly oxygenated ions, $C_2H_3O^+$) values during this period in all three cycles occupy a similar space, previously attributed to SV-OOA and LV-OOA (Ng et al., 2010).

At the peak of the emissions, average oxidation state of carbon (OSc) was in the range of ~ -0.84 to ~ -0.21, while at lower OA concentrations, OSc reached values as high as ~0.5 (Figure SM10b). These average OS_c are significantly higher than what has been observed for fresh and primary vehicle exhaust (with OS_c of ~ -1.65), indicating that OA sampled through TSAR were not similar in composition to that of primary OA (Kroll et al., 2011; Aiken et al., 2008). The OS_c values in the peak of OA concentrations from the FTP and NEDC cycles are however consistent with ambient values in Mexico City, as well as the SV-OOA factor in the ambient data (Kroll et al., 2011; Aiken et al., 2008), suggesting that during the cold-start period of these driving cycles, oxidation conditions of TSAR led to formation of SOA that is representative of those found in urban environments. During the LA92, average OS_c was higher (-0.5 to 0.5), consistent with the more aged ambient OA and LV-OOA factor of the ambient data (Kroll et al., 2011; Aiken et al., 2008). These observations are consistent with a slightly higher OH exposure during the cold-start phase of LA92 compared to the corresponding phase in the FTP and NEDC cycles due to relatively lower emissions of NMHC in LA92 (5 equivalent days in LA92 vs. 3.9-4.3 equivalent days in FTP and NEDC, assuming daily average OH of $1.5x10^6$ molecule/cm^3) (Figure SM2b).

For all the cold-start cycles, SOA formation, as well as SOA precursor emissions (i.e., NMHC), were at least an order of magnitude lower for the hot-running phases compared to the cold-start phase. Higher combustion and exhaust temperatures, and the higher catalytic activity of the TWC resulted in reduced formation and the more efficient oxidation of the emitted precursors for the hot-running phases. It is interesting to note that a sharp peak of SOA formation was detected at the end of the NEDC during the last acceleration that correlates well with the peak of tailpipe NMHC emissions. Similar results were observed in previous studies with gasoline vehicles over the NEDC (Simonen et al., 2019; Simonen et al., 2017).

For both Caltrans cycles, SOA formation was found to depend on driving conditions and oxidation conditions. For Caltrans 1, SOA formation per miles driven was factors of 1.4-3.2 higher during the first two phases that primarily represented slow driving in congested highways than the phases representing steady-state high-speed driving, despite the lower NMHC emissions for the first two phases. However, as shown in Figure SM2 (SM), the steady-state high speed phase had significantly lower OH exposure due to higher CO emissions (Figure SM11), which likely contributed to the lower SOA formation. Similar to Caltrans 1, the first two phases of Caltrans 2 that were characterized by more aggressive, frequent braking, and lower speed driving resulted in factors of 2.2-3.6 more SOA formation compared to the higher speed and free-flow driving of the last two phases of the cycle. Because of the similarity in OH exposure between different phases of Caltrans 2, the higher SOA formation in the more aggressive driving phases suggests higher emissions of SOA precursors during such driving conditions.

Time-series plots of aerosol sulfate indicate relatively low concentrations for all driving cycles and generally its formation was associated with vehicle accelerations. It should be noted that the sulfate aerosol comprised a rather small portion of the total secondary aerosol (less than 1%). This is primarily a consequence of the very tight sulfur standards for gasoline fuels and the very low sulfur levels in lubricant oils. However, even low levels of sulfur in the fuel and the lubricant oil can be stored in the TWC and subsequently released as SO_2 to prompt the formation of SO_3 and the further production of sulfate complexes (Simonen et al., 2019; Maricq et al., 2002). For the LA92 and NEDC, sulfate was seen in higher concentrations (about a factor of two) than the Caltrans cycles, as a result of the cold-start period, which negatively affects fuel impingement and evaporation, increases lubricant oil viscosity, leading to more PM and unburned hydrocarbons. This phenomenon was particularly noticeable over the NEDC, where sulfate aerosol showed

elevated concentrations during the first 100 seconds of the cycle. It is therefore assumed that lubricant oil, in addition to fuel fragments, may have an important role in emissions of secondary aerosol precursors during cold-start operation of GDI engines. For the Caltrans cycles, sulfate aerosol was higher during the lower speed and load conditions, suggesting higher fuel and lubricant oil consumption during congested highway conditions.

There was substantial formation of nitrate for all driving cycles, which exceeded the SOA formation except during the cold-start periods. This finding is in good agreement with previous studies on gasoline vehicles that have reported elevated secondary inorganic aerosol production using either smog chambers or oxidation flow reactors (Vu et al., 2019; Roth et al., 2020; Tkacik et al., 2014). For example, Vu et al. (2019) showed higher inorganic aerosol mass than SOA when they tested four GDI vehicles over the LA92 using an environmental chamber, whereas Tkacik et al. (2014) demonstrated an increased production of ammonium nitrate by a factor of 2 compared to SOA when they deployed a PAM reactor in a highway tunnel in Pittsburgh. The measured nitrate in the current study could stem from presence of inorganic (i.e., ammonium nitrate) and organic nitrates; therefore, it is of interest to understand the contribution of either class of species to the measured aerosol nitrate. The observed ratios of two main fragments of nitrate in mAMS, NO^+/NO_2^+ (R_{obs}), during the cold-start cycles were predominantly in the range of expected values for ammonium nitrate (R_{AN}), suggesting that most of the times, and especially when the nitrate mass fraction relative to OA was greater than ~20%, the observed nitrate was due to formation of ammonium nitrate (Figure 4a). However, as seen in Figure 4b, at moderate absolute concentrations of nitrate and high concentrations of OA (i.e., larger markers in Figure 4(a-b)) during the cold-start, R_{obs} was significantly higher than R_{AN}. This observation suggests that in the beginning of the cold-start cycles, conditions were conducive for organonitrate formation given the high co-

emission of NOx and NMHCs. During the Caltrans cycles, the overall concentrations of OA were significantly lower than during the first phase of the cold-start cycles, and the nitrate mass fractions relative to OA reached values >70%. During these times, R_{obs} was predominantly in the range of R_{AN}, indicating that the fate of the emitted NOx during high-speed driving of the hot-cycles was dominated by oxidation to nitric acid (instead of reactions with peroxy radicals to form organonitrates) and eventual partitioning to aerosols as inorganic nitrate (Figure 5). Overall, there is a good agreement between tailpipe NOx emissions during acceleration and high-speed conditions and nitrate formation. Acceleration events and dynamic driving resulted in higher combustion temperatures and enhanced formation of NOx. Therefore, high-speed highway conditions and aggressive urban driving will likely affect the formation of secondary nitrate aerosol. An exception was observed for the low-speed phase of Caltrans 1, where nitrate showed significantly higher formation compared to the high-speed phase of the cycle despite tailpipe NOx emissions being low.

Ammonium nitrate is not emitted directly from gasoline exhaust. However, secondary ammonium nitrate can be formed in the TSAR from the oxidation of NOx emissions to nitric acid, which then react with gaseous ammonia (NH_3). The limiting reagents in the atmospheric transformation of ammonium nitrate are nitric acid or NH_3 (Link et al., 2017). Although NH_3 emissions were not measured for this vehicle, an attempt was made to correlate ammonium nitrate formation with CO emissions since it is usually positively correlated with NH_3 emissions in spark ignition engines (Suarez-Bertoa et al., 2014). Ammonia can be formed during rich operations in the TWC from NO reduction by elemental H_2 during the water gas shift reaction of CO and hydrocarbon steam reforming (Suarez-Bertoa et al., 2014). A clear correlation between CO emissions and ammonium nitrate was not observed (Figure SM11), since in some cases CO

emissions were low when at the same time ammonium nitrate production was elevated. These findings indicate that ammonium nitrate formation was largely driven by NOx emissions and limited by nitric acid formation rather than ammonia emissions.

3.3 Emission factors

The emission factors (EF), expressed in mg/mile, are shown in Figure 6 and Figure SM12. SOA formation for the cold-start cycles was significantly higher than that for the hot-start cycles, with the milder driving conditions of NEDC generating 2.8 and 7.6 times more SOA than LA92 and FTP, respectively. Cold-start SOA EFs were 31, 13, and 57 times higher than SOA EFs obtained during the hot-running phases of the NEDC, LA92, and FTP, respectively (Table SM2). As previously discussed, SOA EFs were on average 2.3 and 2.9 times higher for the first two phases of Caltrans 1 and Caltrans 2 cycles, respectively, that primarily represent congested highway driving conditions compared to the last two phases that represent high-speed, free-flow highway driving. Nitrate EFs contributed to the largest portion of total secondary aerosol, followed by ammonium. The hot-start Caltrans cycles showed the largest contribution of inorganic aerosol compared to the cold-start cycles, as a result of the higher NOx and NH_3 emissions. Analogous to SOA EFs, nitrate and ammonium EFs were on average 3.9 and 3.6 times higher for the first two phases of Caltrans 1 and 2.5 and 2.6 times higher for the first two phases of Caltrans 2 compared to the last two phases of the Caltrans cycles. The results reported here suggest that more secondary organic and inorganic aerosol will be formed from GDI vehicles when operated under highway congested traffic conditions.

4. Conclusions

The cold-start period generated significant SOA mass, resulting in ~70-80% of the non-refractory mass being SOA. After TWC warmup, contribution of SOA decreased to ~5-12% of the

non-refractory mass while that of nitrate increased from ~15% to ~60-73%. After the cold-start phase, however, total non-refractory mass was also significantly (up to five times) lower than during the cold-start phase. These observations suggest that warming of the TWC is an important factor in reducing emissions of SOA precursors. Furthermore, the influence of vehicle emissions on secondary PM formation, both in terms of concentration and type, changes as the vehicle is driven farther/longer and TWC is warmed up. This suggests that under stagnant and cold conditions, PM exposure of neighborhood residents can be significantly different than those outside the neighborhood.

A notable feature of the data is the significant emissions of nitrate (predominantly ammonium nitrate) in these drive cycles, except for NEDC and FTP runs, with total nitrate emission factors being 4-14 times higher than SOA. It is worth noting though that given the semivolatile nature of ammonium nitrate and its equilibrium with gas phase ammonia and nitric acid, ambient levels of ammonium nitrate may never reach concentrations significantly higher than SOA unless ambient temperature and relative humidity levels are favorable. Regardless, since ammonium nitrate formation is suspected to be nitric acid-limited, controls that further reduce NOx emissions will reduce formation of inorganic PM and improve regional air quality.

Acknowledgements

We acknowledge funding from CARTEEH (Center for Advancing Research in Transportation Emissions, Energy, and Health) and USDA-NIFA Hatch (Project No. CA-R-ENS-5072-H, Accession No. 1015963). Niina Kuittinen acknowledges funding from Tampere University Graduate School and the American-Scandinavian Foundation. Niina Kuittinen and Topi Rönkkö acknowledges funding for the Black Carbon Footprint project, granted by Business Finland, Finnish authorities and companies. The authors thank the late Mr. Kurt Bumiller for helping setting

up the experiment and dedicate this publication to his memory. We thank Mr. Mark Villela and Mr. Daniel Gomez of the University of California, Riverside for their contribution in conducting testing for this research program.

References

Aiken, A. C., DeCarlo, P. F., Kroll, J. H., Worsnop, D. R., Huffman, J. A., Docherty, K. S., Ulbrich, I. M., Mohr, C., Kimmel, J. R., Sueper, D., Sun, Y., Zhang, Q., Trimborn, A., Northway, M., Ziemann, P. J., Canagaratna, M. R., Onasch, T. B., Alfarra, M. R., Prevot, A. S. H.,, Dommen, J.,, Duplissy, J., Metzger, A., Baltensperger, U., Jimenez, J. L. O/C and OM/OC ratios of primary, secondary, and ambient organic aerosols with high-resolution time-of-flight aerosol mass spectrometry. Environ. Sci. Technol. 2008, 42, 4478-4485.

Bahreini, R., Middlebrook, A. M., de Gouw, J. A., Warneke, C., Trainer, M., Brock, C. A., Stark, H., Brown, S. S., Dube, W. P., Gilman, J. B., Hall, K., Holloway, J. S., Kuster, W. C., Perring, A. E., Prevot, A. S. H., Schwarz, J. P., Spackman, J. R., Szidat, S., Wagner, N. L., Weber, R. J., Zotter, P., Parrish, D. D. Gasoline emissions dominate over diesel in formation of secondary organic aerosol mass. Geophys. Res. Lett. 2012a, 39, L06805, doi: 10.1029/2011GL050718.

Bahreini, R., Middlebrook, A. M., Brock, C. A., de Gouw, J. A., McKeen, S. A., Williams, L. R., Daumit, K. E., Lambe, A. T., Massoli, P., Canagaratna, M. R., Ahmadov, R., Carrasquillo, A. J., Cross, E. S., Ervens, B., Holloway, J. S., Hunter, J. F., Onasch, T. B., Pollack, I. B., Roberts, J. M., Ryerson, T. B., Warneke, C., Davidovits, P., Worsnop, D. R., Kroll, J. H. Mass spectral analysis of organic aerosol formed downwind of the deepwater horizon oil spill: Field studies and laboratory confirmations. Environ. Sci. Technol. 2012b, 46, 8025-8034.

Cao, J., Wang, Q., Li, L., Zhang, Y., Tian, J., Antony Chen, L.W., Hang-Ho, S.S., Wang, X., Chow, J.C., Watson, J.G. Evaluation of the oxidation flow reactor for particulate matter emission limit certification. Atmospheric Environment 2020, 224, 117086.

Chen, L., Liang, Z., Zhang, X., Shuai, S. Characterizing particulate matter emissions from GDI and PFI vehicles under transient and cold start conditions. Fuel 2017, 189, 131-140.

Cheng, Y., Wang, J., Zhuang, R., Wu, N. Analysis of combustion behavior during cold-start and warm-up process of SI gasoline engine. SAE Technical Paper 2001, 2001-01-3557.

Collier, S., Zhang, Q. Gas-phase CO2 subtraction for improved measurements of the organic aerosol mass concentration and oxidation degree by an aerosol mass spectrometer. Environ. Sci. Technol. 2013, 47, 14324–14331.

Du, Z., Hu, M., Peng, J., Zhang, W., Zheng, J., Gu, F., Qin, Y., Yang, Y., Li, M., Wu, Y., Shao, M., Shuai, S. Comparison of primary aerosol emission and secondary aerosol formation from gasoline direct injection and port fuel injection vehicles. Atmos. Chem. Phys. 2018, 18, 9011-9023.

Drozd, G.T., Zhao, Y., Saliba, G., Frodin, B., Maddox C., Chang, M.C.O., Maldonado, H., Sardar, S., Weber, R.J., Robinson, A.L., Goldstein, A.H. Detailed speciation of intermediate volatility and semivolatile organic compound emissions from gasoline vehicles: Effects of cold-starts and implications for secondary organic aerosol formation. Environ. Sci. Technol. 2019, 53, 1706-1714.

Duronio, F., De Vita, A., Montanaro, A., Villante, C. Gasoline direct injection engines – A review of latest technologies and trends. Part 2. Fuel 2020, 265, 116947.

Gentner, D.R., Jathar, S.H., Gordon, T.D., Bahreini, R., Day, D.A., Haddad, I.E., Haynes, P.L., Pieber, S.M., Platt, S.M., De Gouw, J., Goldstein, A.H., Harley, R.A., Jimenez, J.L., Prevot,

A.S.H., Robinson A.L. Review of urban secondary organic aerosol formation from gasoline and diesel motor vehicle emissions. Environ. Sci. Technol. 2017, 51, 1074-1093.

Gordon, T. D., Presto, A. A., May, A. A., Nguyen, N. T., Lipsky, E. M., Donahue, N. M., Gutierrez, A., Zhang, M., Maddox, C., Rieger, P., Chattopadhyay, S., Maldonado, H., Maricq, M. M., Robinson, A. L. Secondary organic aerosol formation exceeds primary particulate matter emissions for light-duty gasoline vehicles. Atmos. Chem. Phys. 2014, 14, 4661–4678.

Herrington, J.S., Hays, M.D., George, B.J., Baldauf, R.W. The effects of operating conditions on semivolatile organic compounds emitted from light-duty, gasoline-powered motor vehicles. Atmospheric Environment 2012, 54, 53-59.

Jathar, S.H., Woody, M., Pye, H.O.T., Baker, K.R., Robinson, A.L. Chemical transport model simulations of organic aerosol in southern California: model evaluation and gasoline and diesel source contributions. Atmos. Chem. Phys. 2017, 17, 1-18.

Jayne, J. T., Leard, D. C., Zhang, X., Davidovits, P., Smith, K. A., Kolb, C. E., Worsnop, D. W. Development of an Aerosol Mass Spectrometer for size and composition analysis of submicron particles. Aerosol Sci. Technol. 2000, 33, 49-70.

Jimenez, J. L., Canagaratna, M. R., Donahue, N. M., Prevôt, A. S. H., Zhang, Q., Kroll, J. H., Decarlo, P. F., Allan, J. D., Coe, H., Ng, N. L., Aiken, A. C., Ulbrich, I. M., Grieshop, A. P., Duplissy, J., Wilson, K. R., Lanz, V. A., Hueglin, C., Sun, Y. L., Tian, J., Laaksonen, A., Raatikainen, T., Rautiainen, J., Vaattovaara, P., Ehn, M., Kulmala, M., Tomlinson, J. M., Cubison, M. J., Dunlea, E. J., Alfarra, M. R., Williams, P. I., Bower, K., Kondo, Y., Schneider, J., Drewnick, F., Borrmann, S., Weimer, S., Demerjian, K., Salcedo, D., Cottrell, L., Takami, A., Miyoshi, T., Shimono, A., Sun, J. Y., Zhang, Y. M., Dzepina, K., Sueper, D., Jayne, J. T., Herndon, S. C., Williams, L. R., Wood, E. C., Middlebrook, A. M., Kolb, C. E., Baltensperger,

U., Worsnop, D. R. Evolution of organic aerosols in the atmosphere. Science 2009, 326, 1525-1529.

Kang, E., Root, M., Toohey, D.W., Brune, W.H. Introducing the concept of Potential Aerosol Mass (PAM). Atmos. Chem. Phys. 2007, 7, 5727-5744.

Karjalainen, P., Rönkkö, T., Pirjola, L., Heikkilä, J., Happonen, M., Arnold, F., Rothe, D., Bielaczyc, P., Keskinen, J. Sulfur driven nucleation mode formation in diesel exhaust under transient driving conditions. Environ. Sci. Technol. 2014, 48, 2336-2343.

Karjalainen, P., Timonen, H., Saukko, E., Kuuluvainen, H., Saarikoski, S., Aakko-Saksa, P., Murtonen, T., Dal Maso, M., Ahlberg, E., Svenningsson, B., Brune, W. H., Hillamo, R., Keskinen, J., Rönkkö, T. Time-resolved characterization of primary and secondary particle emissions of a modern gasoline passenger car. Atmos. Chem. Phys. 2016, 16, 8559–8470.

Kari, E., Hao, L., Ylisirnio, A., Buchholz, A., Leskinen, A., Yli-Pirila, P., Nuutinen, I., Kuuspalo, K., Jokiniemi, J., Faiola, C.L., Schobesberger S., Virtanen, A. Potential dual effect of anthropogenic emissions on the formation of biogenic secondary organic aerosol (BSOA). Atmos. Chem. Phys. 2019, 19, 15651-15671.

Kroll, J.H., Seinfeld, J.H. Chemistry of secondary organic aerosol: Formation and evolution of low-volatility organics in the atmosphere. Atmospheric Environment 2008, 42, 3593-3624.

Kroll, J. H., Donahue, N. M., Jimenez, J. L., Kessler, S. H., Canagaratna, M. R., Wilson, K. R., Altieri, K. E., Mazzoleni, L. R., Wozniak, A. S., Bluhm, H., Mysak, E. R., Smith, J. D., Kolb, C. E., Worsnop, D. R. Carbon Oxidation State as a Metric for Describing the Chemistry of Atmospheric Organic Aerosol. Nature Chemistry 2011, 3, 133–139.

Lambe, A.T., Ahern, J.P.D., Brune, W.H., Ng, N.L., Wright, J.P., Croasdale, D.R., Worsnop, D.R., Davidovits, P., Onasch, T.B. Characterization of aerosol photooxidation flow reactors

heterogeneous oxidation, secondary organic aerosol formation and cloud condensation nuclei activity measurements. Atmos. Meas. Tech. 2011, 4, 445-461.

Link, M.F., Kim, J., Park, G., Lee, T., Park, T., Babar, Z.B., Sung, K., Kang, S., Kim, J.S., Choi, Y., Son, J., Lim, H.-J., Farmer, D.K. Elevated production of NH4NO3 from the photochemical processing of vehicle exhaust: Implications for air quality in the Seoul Metropolitan Region. Atmospheric Environment 2017, 156, 95-101.

Liu, T., Wang, X., Deng, W., Hu, Q., Ding, X., Zhang, Y., He, Q., Zhang, Z., Lu, S., Bi, X., Chan, J., Yu, J. Secondary organic aerosol formation from photochemical aging of light-duty gasoline vehicle exhausts in a smog chamber. Atmos. Chem. Phys. 2015, 15, 9049-9062.

Liu, C., Liu, Y., Chen, T., Liu, J., and He, H. Rate constant and secondary organic aerosol formation from the gas-phase reaction of eugenol with hydroxyl radicals. Atmos. Chem. Phys. 2019, 19, 2001-2013.

Maricq, M.M., Chase, R.E., Xu, N., Podsiadlik, D.H. The effects of the catalytic converter and fuel sulfur level on motor vehicle particulate matter emissions: gasoline vehicles. Environ. Sci. Technol. 2002, 36, 276-282.

Maricq, M.M., Szente, J.J., Harwell, A.L., Loos, M.J. Impact of aggressive drive cycles on motor vehicle exhaust PM emissions. Journal of Aerosol Science 2017, 113, 1-11.

Middlebrook, A. M., Bahreini, R., Jimenez, J. L., Canagaratna, M. R. Evaluation of composition-dependent collection efficiencies for the Aerodyne aerosol mass spectrometer using field data. Aerosol Science and Technology 2012, 46, 258-271.

Miersch, T., Czech, H., Stengel, B., Abbaszade, G., Orasche, J., Sklorz, M., Streibel, T., Zimmermann, R. Composition of carbonaceous fine particulate emissions of a flexible fuel DISI engine under high velocity and municipal conditions. Fuel 2019, 236, 1465-1473.

546 Ng, N.L., Canagaratna, M.R., Zhang, Q., Jimenez, J.L., Tian, J., Ulbrich, I.M., Kroll, J.H.,
547 Docherty, K.S., Chhabra, P.S., Bahreini, R., Murphy, S.M., Seinfeld, J.H., Hildebrandt, L.,
548 Donahue, N.M., DeCarlo, P.F., Lanz, V.A., Prevot, A.S.H., Dinar, E., Rudich, Y., Worsnop,
549 D.R. Organic aerosol components observed in Northern Hemispheric datasets from aerosol
550 mass spectrometry. Atmos. Chem. Phys. 2010, 10, 4625-4641.
551 Nordin, E. Z., Eriksson, A. C., Roldin, P., Nilsson, P. T., Carlsson, J. E., Kajos, M. K., Hellén, H.,
552 Wittbom, C., Rissler, J., Löndahl, J., Swietlicki, E., Svenningsson, B., Bohgard, M., Kulmala,
553 M., Hallquist, M., Pagels, J. H. Secondary organic aerosol formation from idling gasoline
554 passenger vehicle emissions investigated in a smog chamber. Atmos. Chem. Phys. 2013, 13,
555 6101-6116.
556 Ortega, A. M., Hayes, P. L., Peng, Z., Palm, B. B., Hu, W., Day, D. A., Li, R., Cubison, M. J.,
557 Brune, W. H., Graus, M., Warneke, C., Gilman, J. B., Kuster, W. C., de Gouw, J., Gutiérrez-
558 Montes, C., Jimenez, J. L. Real-time measurements of secondary organic aerosol formation and
559 aging from ambient air in an oxidation flow reactor in the Los Angeles area, Atmos. Chem.
560 Phys. 2016, 16, 7411–7433.
561 Peng, J., Hu, M., Du, Z., Wang, Y., Zheng, J., Zhang, W., Yang, Y., Qin, Y., Zheng, R., Xiao, Y.,
562 Wu, Y., Lu, S., Wu, Z., Guo, S., Mao, H., Shuai, S. Gasoline aromatics: a critical determinant
563 of urban secondary organic aerosol formation. Atmos. Chem. Phys. 2017, 17, 10743-10752.
564 Pieber, S. M., Kumar, N. K., Klein, F., Comte, P., Bhattu, D., Dommen, J., Bruns, E. A., Kilic, D.,
565 El Haddad, I., Keller, A., Czerwinski, J., Heeb, N., Baltensperger, U., Slowik, J. G., Prévôt, A.
566 S. H. Gas-phase composition and secondary organic aerosol formation from standard and
567 particle filter-retrofitted gasoline direct injection vehicles investigated in a batch and flow
568 reactor. Atmos. Chem. Phys. 2018, 18, 9929-9954.

569 Pirjola, L., Karjalainen, P., Heikkilä, J., Saari, S., Tzamkiozis,T., Ntziachristos, L, Kulmala, K.,
570 Keskinen, J., Rönkkö, T. Effects of Fresh Lubricant Oils on Particle Emissions Emitted by a
571 Modern Gasoline Direct Injection Passenger Car. Environ. Sci. Technol. 2015, 49, 3644−3652.
572 Platt, S. M., El Haddad, I., Zardini, A. A., Clairotte, M., Astorga, C., Wolf, R., Slowik, J. G.,
573 Temime-Roussel, B., Marchand, N., Ježek, I., Drinovec, L., Močnik, G., Möhler, O., Richter,
574 R., Barmet, P., Bianchi, F., Baltensperger, U., Prévôt, A. S. H.: Secondary organic aerosol
575 formation from gasoline vehicle emissions in a new mobile environmental reaction chamber.
576 Atmos. Chem. Phys. 2013, 13, 9141-9158.
577 Platt, S.M., El Haddad, I., Pieber, S.M., Zardini, A.A., Suarez-Bertoa, R., Clairotte, M.,
578 Daellenbach, K.R., Huang, R.-J., Slowik, J.G., Hellebust, S., Temime-Roussel, B., Marchand,
579 N., de Gouw, J., Jimenez, J.L., Hayes, P.L., Robinson, A.L., Baltensperger, U., Astorga, C.,
580 Prévôt, A.S.H. Gasoline cars produce more carbonaceous particulate matter than modern filter-
581 equipped diesel cars. Scientific Reports 2017, 7, 4926, https://doi.org/10.1038/s41598-017-
582 03714-9.
583 Robinson, A. L., Donahue, N. M., Shrivastava, M. K., Weitkamp, E.A., Sage, A. M., Grieshop,
584 A.P., Lane, T. E., Pierce, J. R., Pandis, S. N. Rethinking Organic Aerosols: Semivolatile
585 Emissions and Photochemical Aging. Science 2007, 315, 1259–1262.
586 Roth, P., Yang, J., Stamatis, C., Barsanti, K.C., Cocker, III D.R., Durbin, T.D., Asa-Awuku, A.,
587 Karavalakis, G. Evaluating the relationships between aromatic and ethanol levels in gasoline
588 on secondary aerosol formation from a gasoline direct injection vehicle. Science of the Total
589 Environment 2020, 737, 140333.
590 Saliba, G., Saleh, R., Zhao, Y., Presto, A.A., Lamber, A.T., Frodin, B., Sardar, S., Maldonado, H.,
591 Maddox, C., May, A.A., Drozd, G.T., Goldstein, A.H., Russell, L.M., Hagen, F., Robinson,

592 A.L. Comparison of gasoline direct-injection (GDI) and port fuel injection (PFI) vehicle
593 emissions: Emission Certification standards, cold-start, secondary organic aerosol formation
594 potential, and potential climate impacts. Environ. Sci. Technol. 2017, 51, 6542-6552.
595 Saha, P.K., Reece, S.M., Grieshop, A.P. Seasonally varying secondary organic aerosol formation
596 from in-situ oxidation of near-highway air. Environ. Sci. Technol. 2018, 52, 7192-7202.
597 Sgro, L.A., Sementa, P., Vaglieco, B.M., Rusciano, G., D'Anna, A., Minutolo, P. Investigating the
598 origin of nuclei particles in GDI engine exhausts. Combustion and Flame 2012, 159, 1687-
599 1692.
600 Simonen, P., Saukko, E., Karjalainen, P., Timonen, H., Bloss, M., Aakko-Saksa, P., Rönkkö, T.,
601 Keskinen, J., Dal Maso, M. A new oxidation flow reactor for measuring secondary aerosol
602 formation of rapidly changing emission sources. Atmos. Meas. Tech. 2017, 10, 1519-1537.
603 Simonen, P., Kalliokoski, J., Karjalainen, P., Rönkkö, T., Timonen, H., Saarikoski, S., Aurela, M.,
604 Bloss, M., Triantafyllopoulos, G., Kontses, A., Amanatidis, S., Dimaratos, A., Samaras, Z.,
605 Keskinen, J., Dal Maso, M., Ntziachristos, L. Characterization of laboratory and real driving
606 emissions of individual Euro 6 light-duty vehicles – Fresh particles and secondary aerosol
607 formation. Environmental Pollution 2019, 255, 113175.
608 Suarez-Bertoa, R., Zardini, A.A., Astorga, C. Ammonia exhaust emissions from spark ignition
609 vehicles over the New European Driving Cycle. Atmospheric Environment 2014, 92 43-53.
610 Tkacik, D.S., Lambe, A. T., Jathar, S., Li, X., Presto A.A., Zhao, Y., Blake, D., Meinardi, S.,
611 Jayne, J. T., Croteau, P. L., Robinson, A. L. Secondary organic aerosol formation from in-use
612 motor vehicle emissions using a potential aerosol mass reactor. Environ. Sci. Technol. 2014,
613 48, 11235-11242.

Vu, K. T., Dingle, J. H., Bahreini, R., Reddy, P. J., Apel, E. C., Campos, T. L., DiGangi, J. P., Diskin, G. S., Fried, A., Herndon, S. C., Hills, A. J., Hornbrook, R. S., Huey, G., Kaser, L., Montzka, D. D., Nowak, J. B., Pusede, S. E., Richter, D., Roscioli, J. R., Sachse, G. W., Shertz, S., Stell, M., Tanner, D., Tyndall, G. S., Walega, J., Weibring, P., Weinheimer, A. J., Pfister, G., Flocke, F. Impacts of the Denver Cyclone on regional air quality and aerosol formation in the Colorado Front Range during FRAPPÉ 2014. Atmos. Chem. Phys. 2016, 16, 12039-12058.

Vu, D., Roth, P., Berte, T., Yang, J., Cocker D., Durbin T., Karavalakis, G., Asa-Awuku, A. Using a new Mobile Atmospheric Chamber (MACh) to investigate the formation of secondary aerosols from mobile sources: The case of gasoline direct injection vehicles. Journal of Aerosol Science 2019, 133, 1-11.

Yang, J., Roth, P., Ruehl, C.R., Shafer, M.M., Antkiewicz, D.S., Durbin, T.D., Cocker, D., Asa-Awuku, A., Karavalakis, G. Physical, chemical, and toxicological characteristics of particulate emissions from current gasoline direct injection vehicles. Science of the Total Environment 2019a, 650, 1182-1194.

Yang, J., Roth, P., Zhu, H., Durbin, T.D., Karavalakis, G. Impacts of gasoline aromatic and ethanol levels on the emissions from GDI vehicles: Part 2. Influence on particulate matter, black carbon, and nanoparticle emissions. Fuel 2019b, 252, 812-820.

Zhang, Y., Deng, W., Hu, Q., Wu, Z., Yang, W., Zhang, H., Wang, Z., Fang, Z., Zhu, M., Li, S., Song, W., Ding, X., Wang, X. Comparison between idling and cruising gasoline vehicles in primary emissions and secondary organic aerosol formation during photochemical ageing. Science of the Total Environment 2020, 722, 137934.

635 Zhao, Y., Saleh, R., Saliba, G., Presto, A.A., Gordon, T.D., Drozd, G.T., Goldstein, A.H.,
636 Donahue, N.M., Robinson, A.L. Reducing secondary aerosol formation from gasoline vehicle
637 exhaust. Proc Natl Acad Sci USA 2017, 114, 6984-6989.
638 Zhao, Y., Lamber, A.T., Saleh, R., Saliba, G., Robinson, A.L. Secondary organic aerosol
639 production from gasoline vehicle exhaust: Effects of engine technology, cold start, and emission
640 certification standard. Environ. Sci. Technol. 2018, 52, 1253-1261.
641 Zimmerman, N., Rais, K., Jeong, C.H., Pant, P., Delgado-Saborit, J.M., Wallace, J.S., Evans, G.J.,
642 Brook, J.R., Godri Pollitt, K.J. Carbonaceous aerosol sampling of gasoline direct injection
643 engine exhaust with an integrated organic gas and particle samples. Science of the Total
644 Environment 2019, 652, 1261-1269.

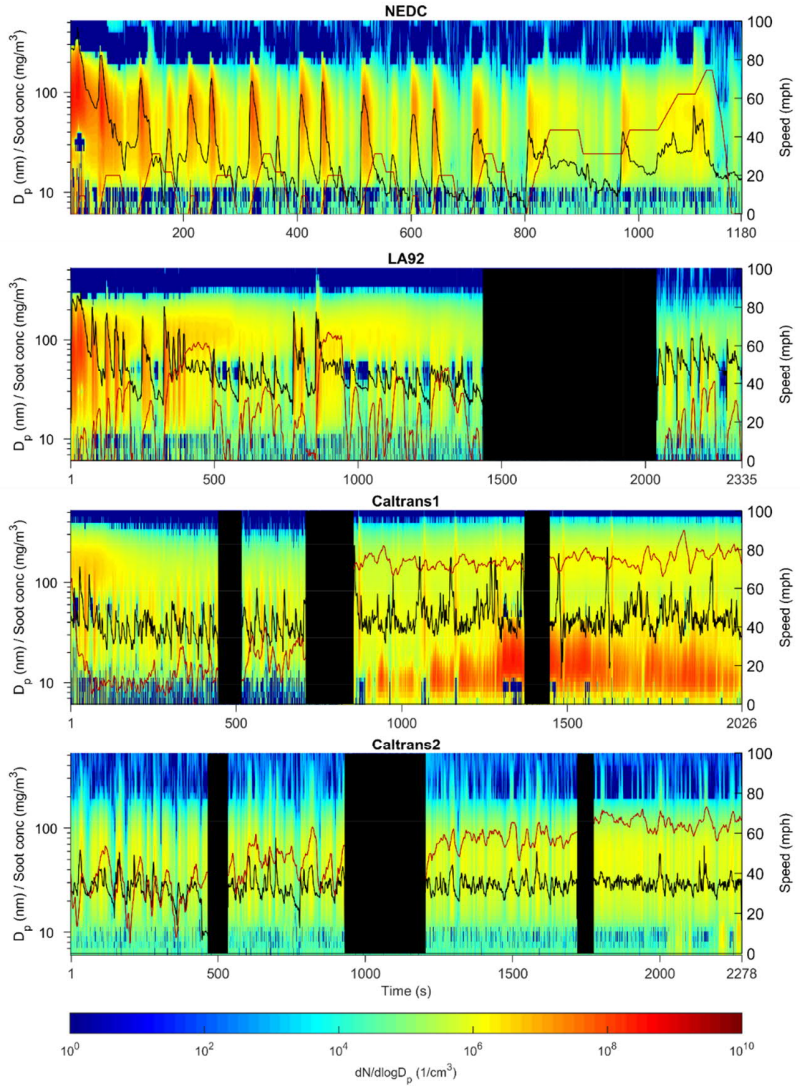

645

646 **Figure 1.** Particle size distributions measured by EEPS shown as heatmap together with soot
647 concentrations measured by MSS (black line, left y-axis, note logarithmic scale), and vehicle speed
648 (red line, right y-axis). The values are corrected to represent tailpipe concentrations. Transition
649 and soak periods between different phases of the cycle have been omitted. Shown concentrations
650 have been corrected by dilution to represent tailpipe concentrations. Results are averages from
651 repeatable duplicate runs, except for Caltrans 1, which was a single run.

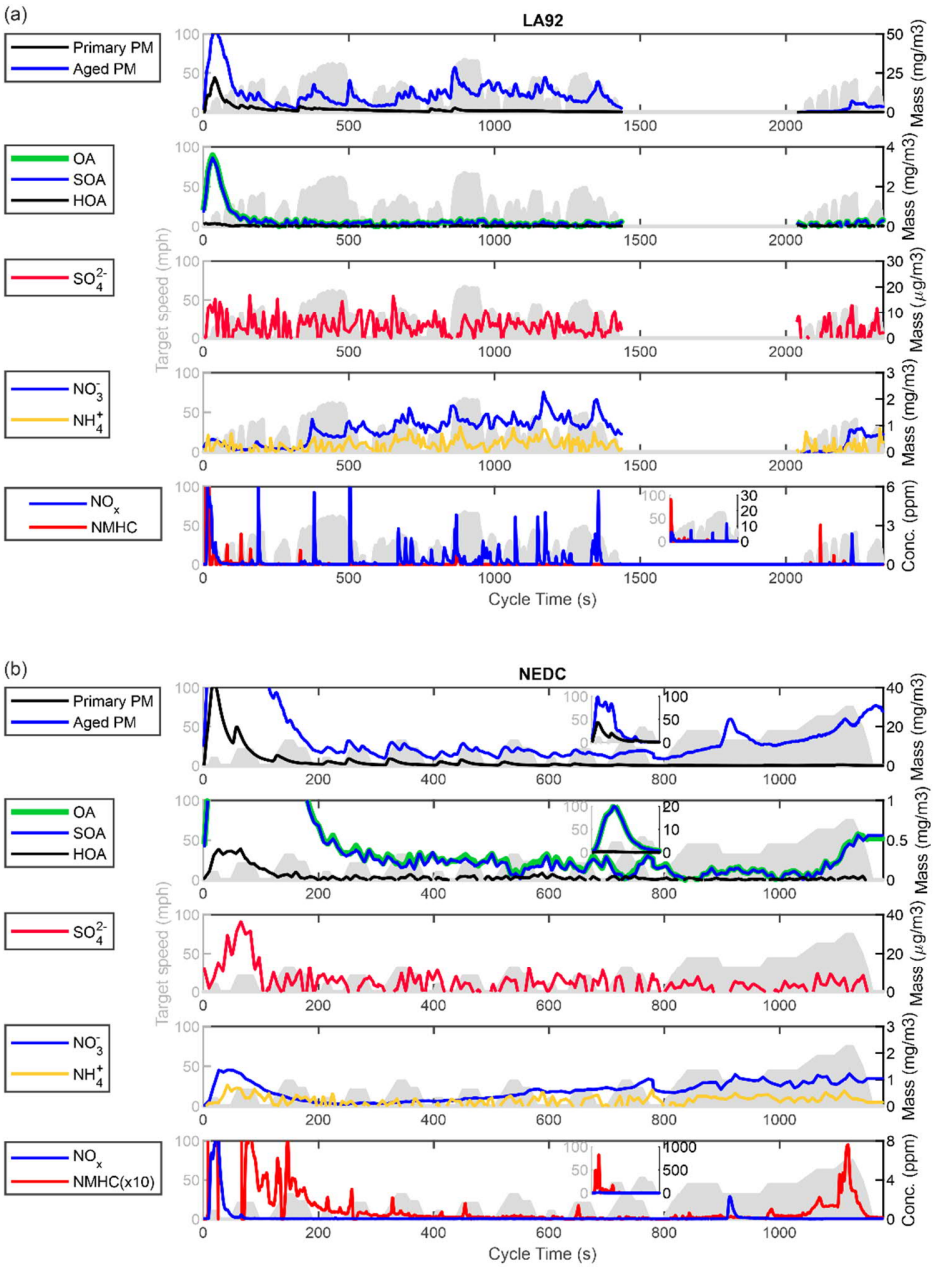

652

653 **Figure 2.** Time-series of primary (measured by EEPS) and aged (measured by ELPI+) PM, SOA,
654 sulfate, ammonium and nitrate ions (measured by mAMS), and tailpipe NMHC and NOx
655 concentrations over the LA92 and NEDC cycles. For comparison, primary PM measured by EEPS
656 is shown corrected with time convolution caused by residence time in the TSAR chamber.
657 Subfigures inside the plots show concentrations during the cold starts, for NEDC during the first

200s, and, for LA92 during the first 600s of the cycle. Shown concentrations have been corrected by dilution to represent tailpipe concentrations. Results are averages from repeatable duplicate runs, except for Caltrans 1, which was a single run.

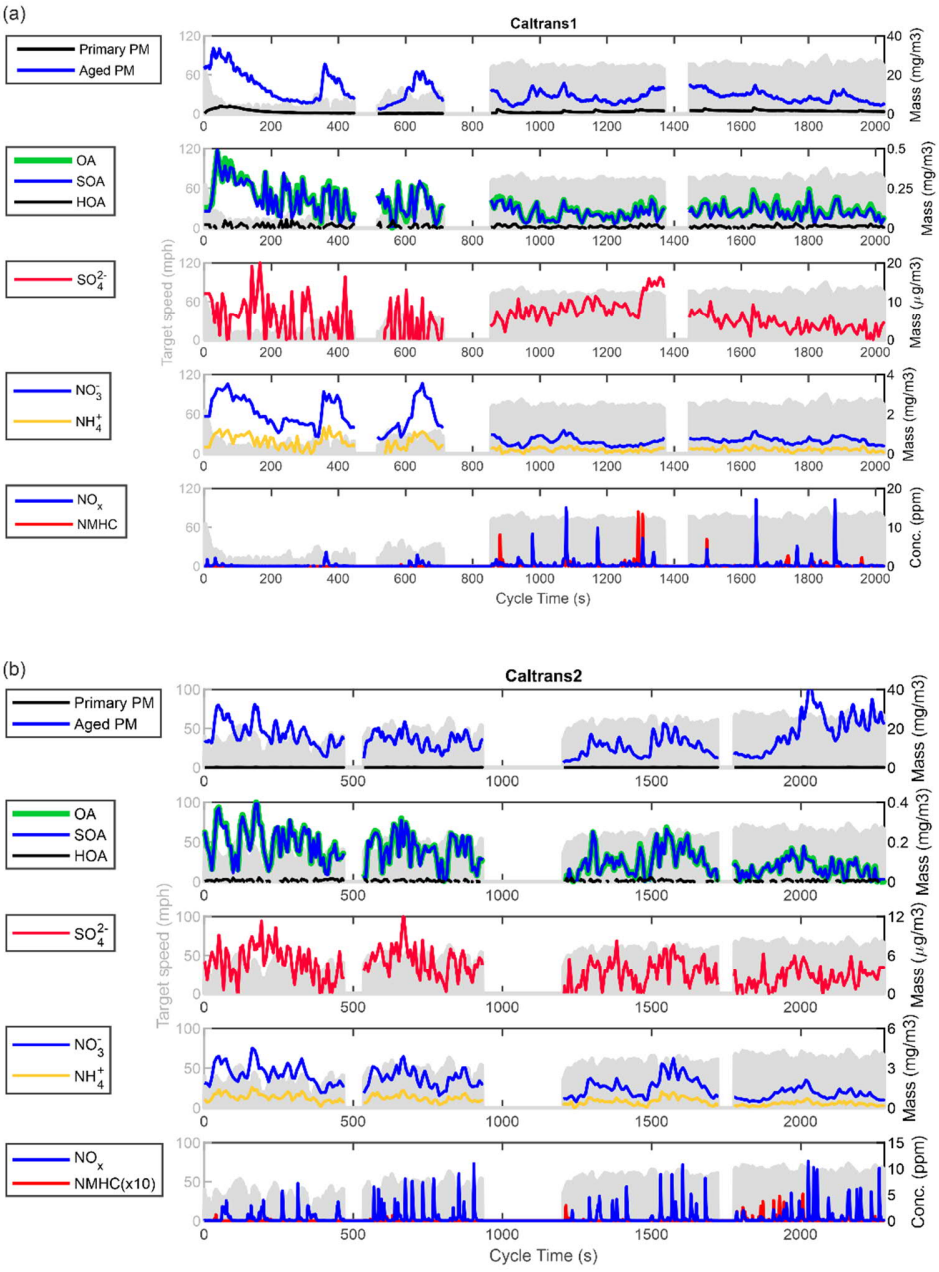

Figure 3. Time-series of primary (measured by EEPS) and aged (measured by ELPI+) PM, SOA, sulfate, ammonium and nitrate ions (measured by mAMS), and tailpipe NMHC and NOx concentrations over the Caltrans 1 and Caltrans 2 cycles. For comparison, primary PM measured by EEPS is shown corrected with time convolution caused by residence time in the TSAR chamber.

667 Shown concentrations have been corrected by dilution to represent tailpipe concentrations. Results
668 are averages from repeatable duplicate runs, except for Caltrans 1, which was a single run.
669

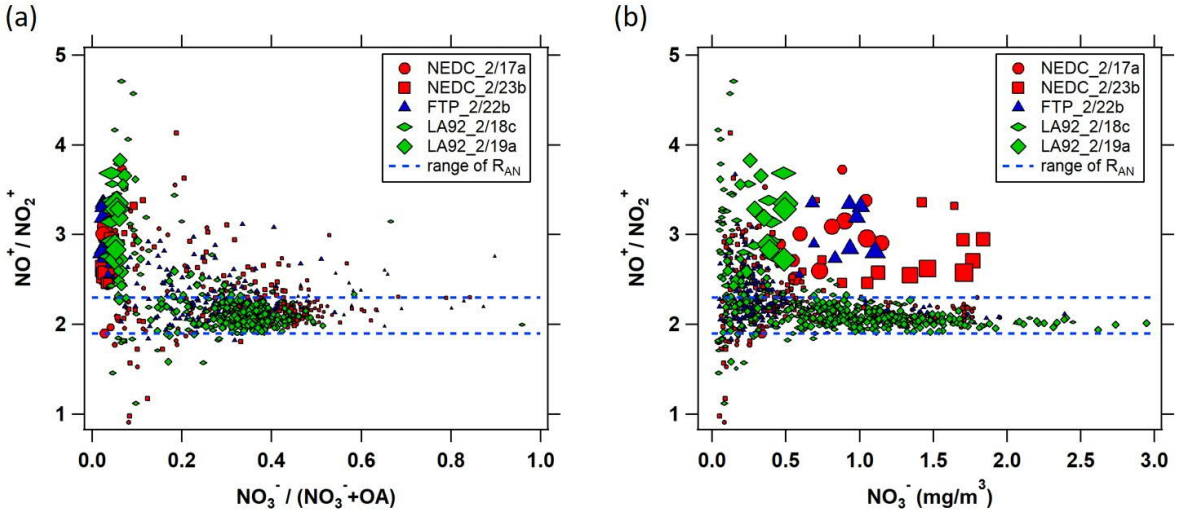

670

671 **Figure 4**. Observed high-resolution NO^+/NO_2^+ ratio during the full cold-start cycles of NEDC,

672 FTP, and LA92 runs, as a function of (a) nitrate fraction relative to OA; (b) total measured nitrate.

673 Data points are sized to the maximum OA value in each run.

674

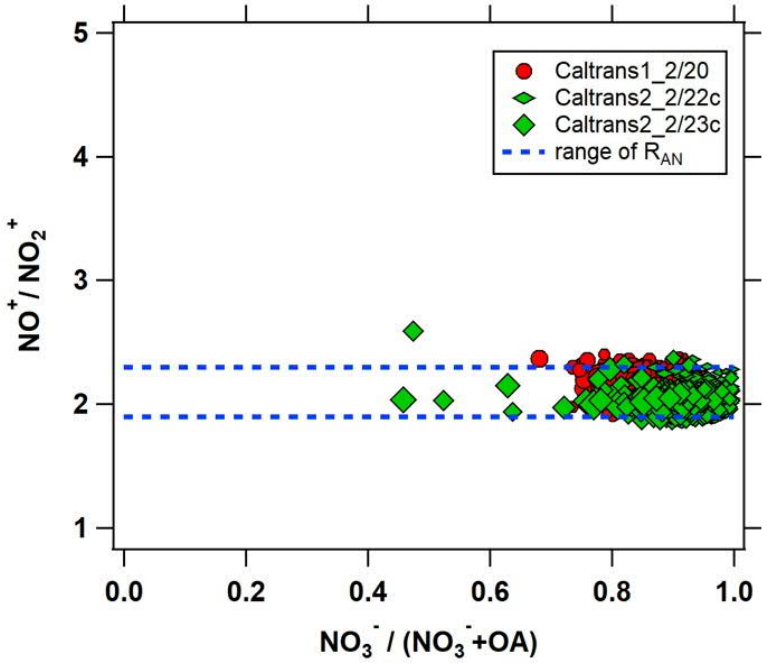

675

676 **Figures 5.** Observed high-resolution NO^+/NO_2^+ ratio during the hot-start Caltrans 1 and Caltrans

677 2 runs, as a function of nitrate fraction relative to OA. Data points are sized to the maximum OA

678 value in each run.

679

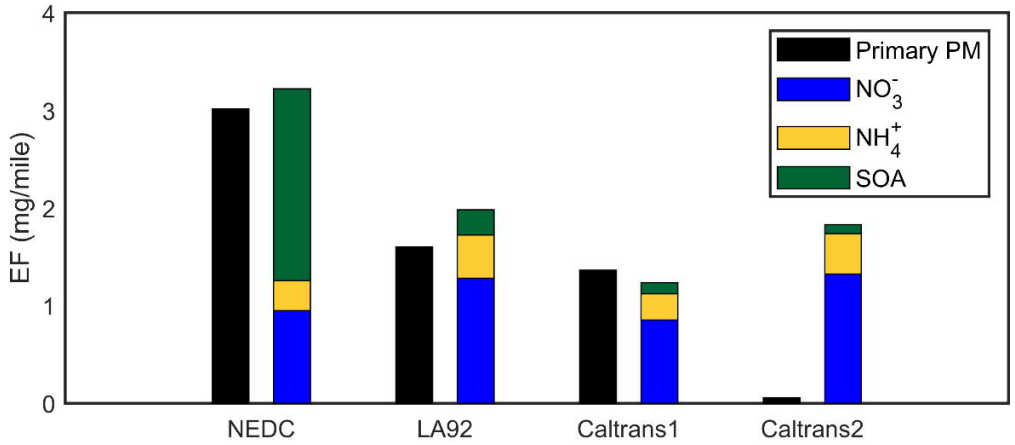

680

681 **Figure 6**. Emission factors for primary PM measured by EEPS and aged NO_3^-, NH_4^+, and SOA
682 measured by AMS for NEDC, LA92, Caltrans 1, and Caltrans 2 cycles. Results are averages from
683 repeatable duplicate runs, except for Caltrans 1, which was a single run.